Received: 4 December 2023 | Revised: 6 January 2024 | Accepted: 19 January 2024

DOI: 10.1002/agt2.514

Aggregate WILEY

RESEARCH ARTICLE

Supramolecular phthalocyanine assemblies-enhanced synergistic photodynamic and photothermal therapy guided by photoacoustic imaging

Yuan-Yuan Zhao[1,2] | **Xiaojun Zhang**[1] | **Zixuan Chen**[1] | **Yihui Xu**[1] | **Heejeong Kim**[2] | **Hyunsun Jeong**[2] | **You Rim Lee**[2] | **Jiah Lee**[2] | **Xingshu Li**[1] | **Juyoung Yoon**[2]

[1]Fujian Provincial Key Laboratory of Cancer Metastasis Chemoprevention and Chemotherapy, College of Chemistry, Fuzhou University, Fuzhou, China

[2]Department of Chemistry and Nanoscience, Ewha Womans University, Seoul, South Korea

Correspondence
Xingshu Li, Fujian Provincial Key Laboratory of Cancer Metastasis Chemoprevention and Chemotherapy, College of Chemistry, Fuzhou University, Fuzhou 350108, China.
Email: xingshuli@fzu.edu.cn

Juyoung Yoon, Department of Chemistry and Nanoscience, Ewha Womans University, Seoul 03760, Korea.
Email: jyoon@ewha.ac.kr

Funding information
National Natural Science Foundation of China, Grant/Award Numbers: 22078066, T2322004; National Research Foundation of Korea, Grant/Award Number: 2022R1A2C3005420; Ewha Womans University

Abstract

Phototherapeutic nanoplatforms that combine photodynamic therapy (PDT) and photothermal therapy (PTT) with the guidance of photoacoustic (PA) imaging are an effective strategy for the treatment of tumors, but establishing a universal method for this strategy has been challenging. In this study, we present a supramolecular assembly strategy based on Förster resonance energy transfer to construct a supramolecular nanostructured phototherapeutic agent (PcDA) via the anion and cation supramolecular interaction between two water-soluble phthalocyanine ramifications, PcD and PcA. This approach promotes the absorption of energy, thus enhancing the generation of reactive oxygen species (ROS) and heat by PcDA, improving its therapeutic efficacy, and overcoming the low photon utilization efficiency of conventional PSs. Notably, after the intravenous injection of PcDA, neoplastic sites could be clearly visualized using PA imaging, with a PA signal-to-liver ratio as high as 11.9. Due to these unique features, PcDA exhibits excellent antitumor efficacy in a preclinical model at a low dose of light irradiation. This study thus offers a general approach for the development of efficient phototherapeutic agents based on the simultaneous effect of PDT and PTT against tumors with the assistance of PA imaging.

KEYWORDS

Förster resonance energy transfer, photoacoustic imaging, photodynamic therapy, photothermal therapy, supramolecular assembly

1 | INTRODUCTION

The spatial heterogeneity of tumors, including changes in pH, enzyme expression, and oxygenation, is a universal pathological characteristic of tumor microenvironments, leading to tumor metastasis and recurrence.[1–4] In particular, heterogeneity in low oxygen (O_2) levels is closely associated with tumor proliferation and invasion, while also promoting drug resistance and attenuating the therapeutic efficacy of other treatment options.[5,6] Due to its minimal invasiveness and spatiotemporal selectivity, photodynamic therapy (PDT) has emerged as a promising strategy for the clinical treatment of cancer and other diseases.[7–9] In PDT, photosensitizers (PSs) together with light irradiation of a suitable wavelength are employed to interact with O_2 to generate cytotoxic reactive oxygen species (ROS), which can induce apoptosis and/or necrosis-induced cell death in tumor tissues.[7,9,10] Thus, PDT is an oxygen-reliant process, which limits its efficiency due to the spatial heterogeneity of O_2 tension in tumor.[11–14] Therefore, the combination of PDT with other treatment techniques is extensively considered an effective solution to robust treatment actions.

Photothermal therapy (PTT), in which PSs utilize light to generate localized heat without consuming O_2 in order to kill pathologic cells, has been developed.[9,15–18] Therefore, the synergistic combination of PDT and PTT, which are both based on the photoirradiation of PSs, has been recognized as an ideal treatment to enhance treatment efficacy.[19] In this system, PTT can conquer the hypoxia limitations of PDT due to its oxygen-independent nature,[20] while the PSs employed for PTT are also capable of ultrasound-based photoacoustic (PA) imaging, a promising biomedical imaging technology with deep tissue penetration.[21–23] Consequently, designing a PS that combines PDT and PTT guided by PA

This is an open access article under the terms of the Creative Commons Attribution License, which permits use, distribution and reproduction in any medium, provided the original work is properly cited.
© 2024 The Authors. *Aggregate* published by SCUT, AIEI and John Wiley & Sons Australia, Ltd.

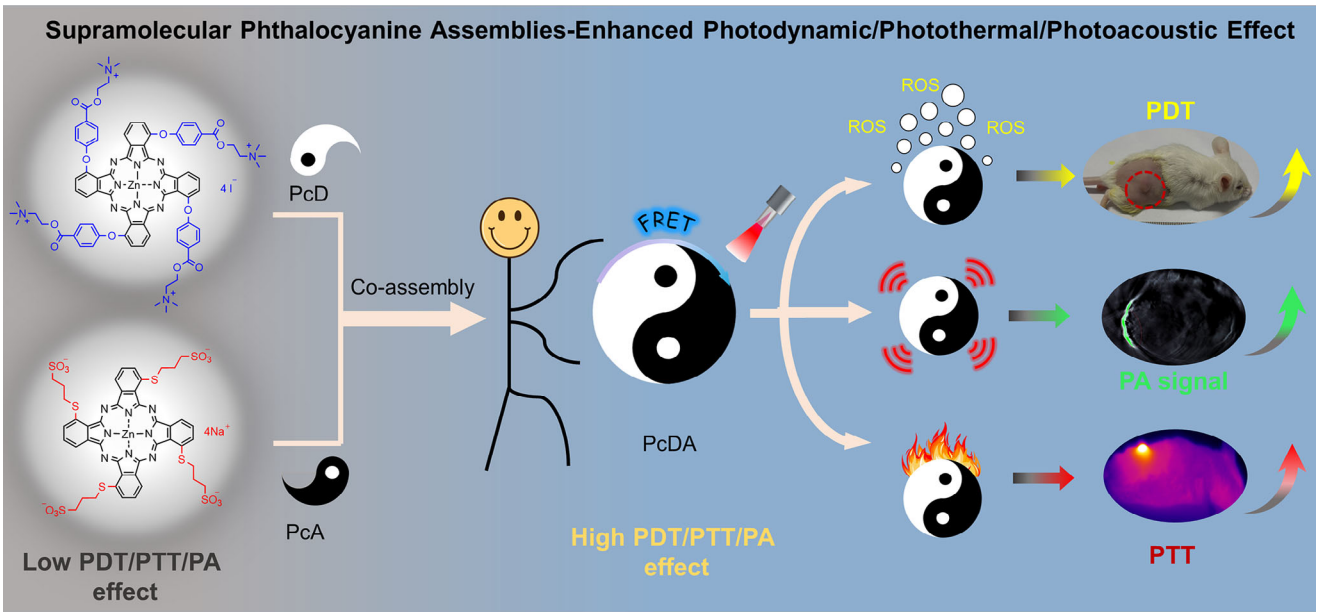


FIGURE 1 Schematic illustration of the fabrication of a nanostructured contrast agent based on the supramolecular interaction between PcD and PcA and its enhanced photodynamic, photothermal, and photoacoustic properties.

imaging represents a potentially useful approach for boosting the tumor treatment effect. To date, a number of near-infrared (NIR) range optical agents, including single molecules (i.e., cyanine, porphyrin, and boron dipyrromethene) or multiple components (i.e., chlorin e6 and gold nanorods),[24–31] have been developed for synergistic PDT and PTT. However, the majority of single-molecule optical agents employed in clinical research or studied in preclinical trials to generate ROS and heat are composed of a poor hydrophilic conjugated structure, which restricts their further range of potential applications.[32,33] For multiple-component optical agents, their complicated preparation process, undesirable metabolic time (some are even prepared by non-biodegradable inorganic materials), and high cost/benefit ratio have also restricted their clinical translation.[34–36]

Recently, supramolecular chemistry has attracted significant attention because it provides a bottom-up strategy for the construction of functional nanoscale materials for biomedical applications.[18,37–40] An amount of noncovalent interactions, including $\pi-\pi$ stacking, van der Waals interactions, hydrophobic effect, hydrogen bonding, and host−guest interactions, have been extensively explored in supramolecular chemistry.[41–44] Along this line, we propose in the present study a facile strategy for the direct assembly of two water-soluble phthalocyanine ramifications to construct a nanostructured phototherapeutic agent for simultaneous PDT and PTT guided by PA imaging. It is believed that a new phototherapeutic agent of this type, developed using a supramolecular self-assembly method based on the Förster resonance energy transfer (FRET) mechanism, would address the shortcomings of existing biomedical limitations.

In this contribution, two water-soluble phthalocyanines, zinc(II) phthalocyanine tetra-substituted with quaternary ammonium salt groups using "oxygen bridge" as the linkages (PcD) and zinc(II) phthalocyanine tetra-substituted with sulphonate groups using "sulfur bridge" as the linkages (PcA), are chosen as the host and guest for the supramolecular assembly (Figure 1). The electrostatic adsorption interaction between PcD (as the cation) and PcA (as the anion) permits spontaneous assembly to constitute uniform nanoparticles in water (PcDA). Encouragingly, the assembly of PcD and PcA leads to efficient energy transfer from PcD to PcA to boost ROS and heat generation upon light irradiation. PcDA also demonstrates an amplified PA signal relative to the PA signal of pure PcD and pure PcA. Notably, PcDA can efficiently visualize the tumor with high contrast in a preclinical model, with a PA signal-to-liver ratio as high as 11.9. Based on these merits, tumor inhibition is achieved in a preclinical model when PcDA is employed in synergistic photodynamic and photothermal tumor therapy, and 95% of the tumor growth was suppressed at a PcDA dose of 0.8 nmol g^{-1} and a light dose of 300 J cm^{-2}.

2 | RESULTS AND DISCUSSION

2.1 | Design and electrostatic adsorption interaction of two water-soluble phthalocyanine molecules and their spectroscopic properties

Phthalocyanines are macrocyclic conjugated organic molecules that have been extensively developed for use as PSs in fluorescence imaging and PDT because their alterable photochemical properties can be adjusted using facile chemical modifications.[45–49] However, only a few investigations to date have employed phthalocyanines in simultaneous PDT and PTT guided by PA imaging. In addition, the majority of previously reported phthalocyanine-based therapies have relied on the fabrication of nanohybrid systems that require hydrophobic phthalocyanines and other additional complex materials,[50,51] and these systems generally suffer from poor fabrication reproducibility, insufficient reagent loads, and unpredictable toxicity. Similar concerns are also associated with most other inorganic nanoparticle-based or organic dye-based systems that have been employed as PSs for PTT and PA imaging. We thus attempted to employ

26924560, 2024, 3, Downloaded from https://onlinelibrary.wiley.com/doi/10.1002/agt2.514 by Ewha Womans University Library, Wiley Online Library on [17/11/2024]. See the Terms and Conditions (https://onlinelibrary.wiley.com/terms-and-conditions) on Wiley Online Library for rules of use; OA articles are governed by the applicable Creative Commons License

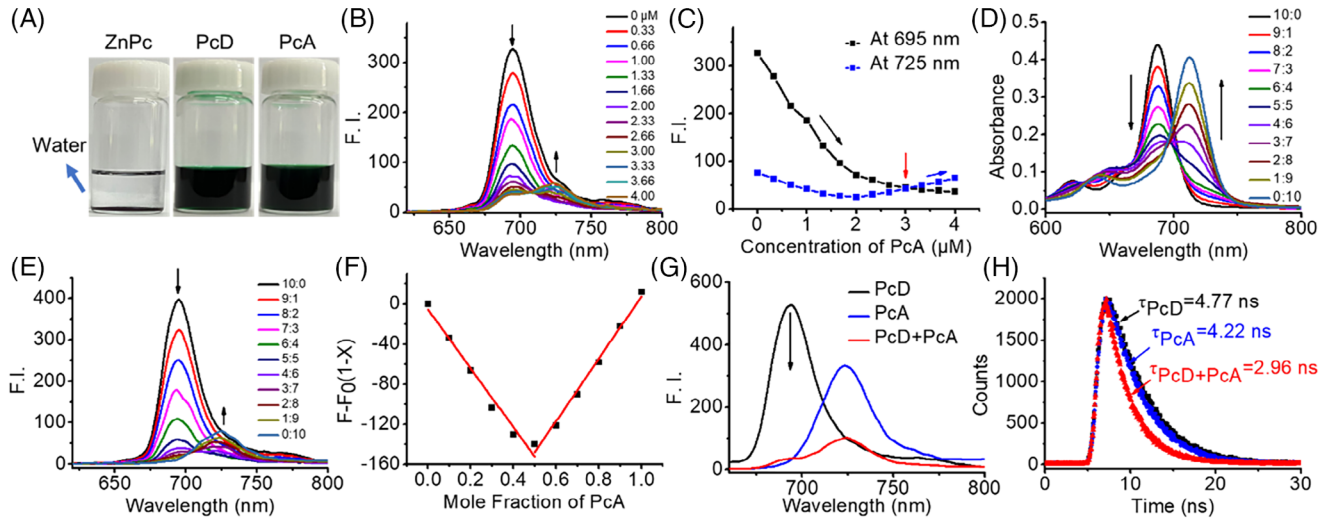


FIGURE 2 (A) The images of ZnPc, PcD, and PcA (all at 8 mg) in water (1 mL). (B) Fluorescence spectra (excited at 610 nm) of PcD (3 μM) with different concentrations of PcA in DMF with 10% water. (C) Fluorescence intensity at 695 and 725 nm of PcD (3 μM) with different concentrations of PcA in DMF with 10% water. (D) Absorbance and (E) fluorescence spectra (excited at 610 nm) of a mixture of PcD and PcA at different ratios. The total concentration of PcD and PcA was fixed at 3 μM. (F) Job plot for the binding of PcD with PcA. (G) Fluorescence (excited at 655 nm) spectra of a mixture of PcD and PcA (v/v = 1:1, total concentration 3 μM), PcD, and PcA (all at 3 μM) in DMF with 10% water. F.I., fluorescence intensity. (H) Fluorescence decay curves of a mixture of PcD and PcA (v/v = 1:1), PcD, and PcA.

supramolecular self-assembly as a specific and green approach for the development of optical agents for biomedical applications. In addition, as one of the most effective strategies to enhance the NIR absorbance capacity of organic PSs, FRET has been widely used to enhance the efficacy of cancer therapies.[52,53] For example, Peng et al. presented a novel strategy employing the single-molecule FRET theory to convert a proportion of fluorescence energy into heat for enhanced photodynamic and photothermal synergistic therapy.[54] Inspired by this, we speculated that a nanostructured assembly of phthalocyanines based on the FRET mechanism may be an effective and universal method for the development of new contrast agents to achieve simultaneous PDT and PTT guided by PA imaging. As a proof of concept, PcD bearing cationic substituents using "oxygen bridge" as the linkages and PcA bearing anionic substituents using "sulfur bridge" as the linkages were selected for this effort.

In the development of our proposed treatment system, the spectral properties of PcD and PcA were first studied in *N,N*-dimethylformamide (DMF). As shown in Figures S1 and S2 and Table S1, not only a sharp Q band but also a shoulder peak was observed for PcD and PcA. In addition, the intensity of the Q band increases linearly with increased concentrations following the Beer–Lambert,[55] implying that PcD and PcA do not aggregate in DMF. Thereafter, the water-solubility of PcD and PcA was evaluated first, with non-substituted zinc(II) phthalocyanine (ZnPc) employed as the control. As shown in Figure 1A, 8 mg of PcD and PcA were completely dissolved in water (1 mL), while ZnPc was insoluble in water in the same environment. Meanwhile, the hydrophilic–hydrophobic properties of these zinc(II) phthalocyanines were compared by measuring their phosphate buffer saline (PBS)/octanol partition coefficient ($P_{w/o}$). As exhibited in Table S2, the log $P_{w/o}$ values for PcD and PcA were −2.37 and −1.96, respectively, which was much lower than that of ZnPc (+2.35). These results indicate that both PcD and PcA have good water-solubility. The binding affinity between PcD and PcA was then analyzed using fluorescence titration. Interestingly, when we increased the equivalent of PcA added to PcD, the fluorescence intensity of PcD at 695 nm gradually decreased (Figure 2B). After adding 1 equivalent of PcA to PcD, the fluorescence intensity at 725 nm exhibited the greatest change (Figure 2C), illustrating the obvious interaction between PcD and PcA. Then, we also employed fluorescence titration to verify their binding stoichiometry. The results presented in Figure 2D,E indicated that PcD bound strongly to PcA, with a binding stoichiometry of 1:1 calculated using a Job plot (Figure 2F).

A clear spectral overlap between the fluorescence emission of PcD and the absorption of PcA can be observed in Figure S3, indicating the potential for FRET to occur between the two as a donor-acceptor pair. In order to better understand the FRET process involving PcD and PcA, we selected different excitation wavelengths (610 and 655 nm) to study the fluorescence emissions of a PcD and PcA (v/v = 1:1) mixture and PcD and PcA alone. As shown in Figure S4, with excitation at 610 nm, energy donor PcD demonstrated intense emission at 695 nm. However, the emissions of both the donor unit PcD and acceptor unit PcA were almost fully quenched in the mixture of PcD and PcA, suggesting that the energy transferred between PcD and PcA was very weak under excitation at 610 nm. In contrast, with excitation at 655 nm, the emission of PcD was almost completely quenched in the mixture of PcD and PcA due to the presence of an energy acceptor, but that of PcA was not quenched at 725 nm, suggesting that efficient energy transfer occurred between PcD and PcA (Figure 2G). The mixture of PcD and PcA (v/v = 1:1) also had a shorter fluorescence lifetime than PcD, providing more evidence that efficient energy transfer took place between PcD and PcA (Figure 2H).

2.2 | Supramolecular self-assembly in water

The self-assembly of PcD and PcA was measured using dynamic light scattering (DLS) in water. As shown in

26924560, 2024, 3, Downloaded from https://onlinelibrary.wiley.com/doi/10.1002/agt2.514 by Ewha Womans University Library, Wiley Online Library on [17/11/2024]. See the Terms and Conditions (https://onlinelibrary.wiley.com/terms-and-conditions) on Wiley Online Library for rules of use; OA articles are governed by the applicable Creative Commons License

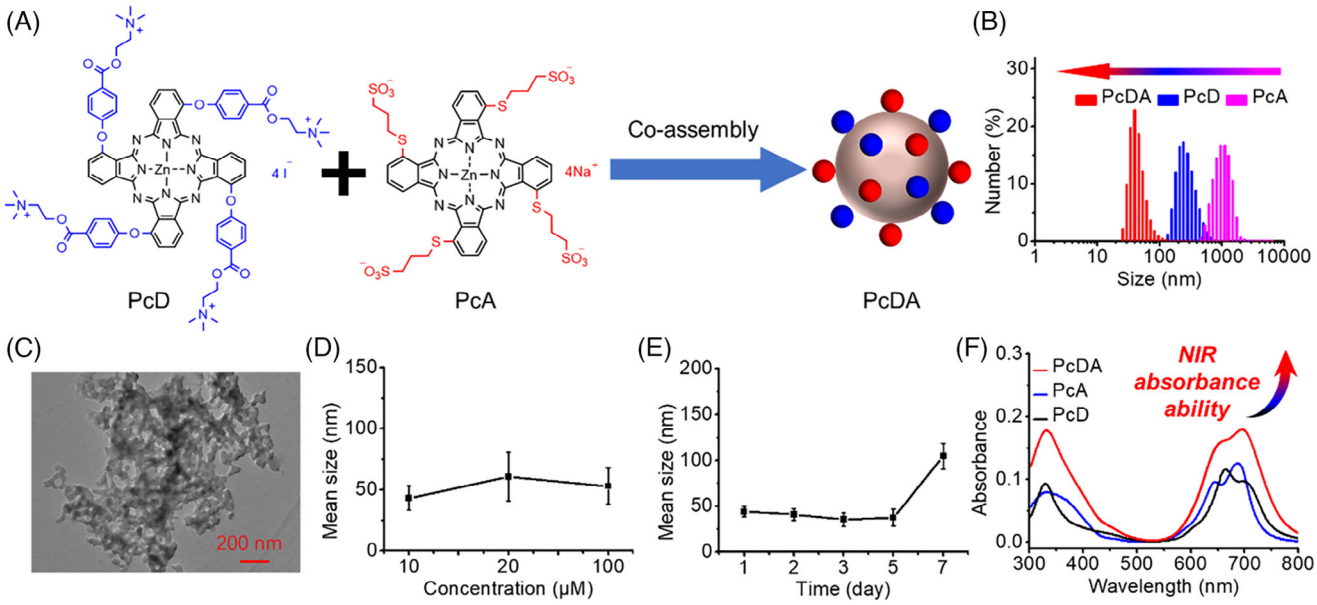


FIGURE 3 Preparation and characterization of the nanostructured supramolecular assemblies. (A) Schematic illustration of PcD and PcA co-assembly to form PcDA. (B) Size distribution of PcDA (the total concentration of PcD and PcA was fixed at 10 μM, v/v = 1:1), PcD, and PcA (all at 10 μM) in water detected by DLS. (C) Morphology of PcDA determined using TEM. (D) DLS particle size profiles for different concentrations of PcDA. (E) Mean particle size of PcDA (10 μM) in water after aging for different times detected using DLS. (F) Absorption spectra of PcDA (the total concentration of PcD and PcA was fixed at 3 μM, v/v = 1:1), PcD, and PcA (all at 3 μM) in water.

Figure 3A,B, although PcD and PcA have good water solubility, pure PcD and PcA (both at 10 μM) exhibited some aggregation in water, with hydrodynamic diameters of more than 500 nm. However, mixing PcD and PcA (v/v = 1:1, total concentration 10 μM) in an aqueous solution generated assemblies with hydrodynamic diameters of about 60 nm, revealing that PcDA nanoassemblies had formed. Subsequent transmission electron microscopy (TEM) revealed that PcDA was present primarily as oval-shaped nanoparticles (Figure 3C). Collectively, these results indicated that PcD and PcA could be used not only as a donor-acceptor pair for energy transfer but also as a host–guest pair for the formation of nanostructures via supramolecular self-assembly. In addition, the DLS results also indicated that PcD and PcA (v/v = 1:1) could self-assemble to form a PcDA dispersion at different concentrations (10, 20, and 100 μM) with similar particle sizes (Figure 3D). Stability is an important element in detecting the further biomedical application of PSs. Encouragingly, PcDA demonstrated remarkable dispersion stability because the mean size and the electronic absorption and fluorescence emission intensity of PcDA exhibited no obvious change while in aqueous solution after being placed in the dark for 7 days (Figure 3E and Figure S5). Furthermore, PcDA exhibited relative stability of electronic absorption and fluorescence emission intensity in PBS after aging in the dark for 7 days. Significantly, compared to pure PcD and pure PcA in water, PcDA demonstrated a broader and stronger absorption band ranging (500–800 nm) due to the spectral overlap of PcD and PcA (Figure 3F). Moreover, as exhibited in Figure S6 and Table S3, the extinction coefficient (ε) value of PcDA (58,000 M^{-1} cm^{-1}) was dramatically increased compared to pure PcD (40,000 M^{-1} cm^{-1}) and pure PcA (31,000 M^{-1} cm^{-1}). These results confirmed that the NIR absorbance capability of PcDA was significantly enhanced relative to pure PcD and pure PcA because of the FRET effect, which is conducive to its further applications.

2.3 | FRET-amplified ROS generation and vibrational relaxation-induced photothermal conversion

Generally, the photons absorbed by a PS can be liberated via three different pathways, including fluorescence, undergoing intersystem crossing (ISC) to generate triplet state formation that promotes ROS generation, and utilizing vibrational relaxation to generate heat. As exhibited in Figure 4A, the fluorescence emission of PcDA was almost completely quenched in water only when compared with a mixed solution of DMF and water (v/v = 9:1), indicating that PcDA has great potential for use as an efficient PS for PDT and PTT. The ROS generation capacity of PcDA was also evaluated employing an ROS detector, 2′,7′-dichlorofluorescein diacetate (DCFH-DA). Two different wavelengths of light (655 and 690 nm) were employed in this analysis as excitation sources due to the broad band of PcDA. In contrast to the rapid and large increase in the fluorescence intensity of DCFH-DA with PcDA after exposure to 655 nm light for 100 s, its fluorescence intensity in pure PcD and pure PcA was lowed and increased relatively slowly (Figure 4B and Figure S7). Specifically, the ROS generation ability of PcDA was 4- and 10-fold higher than that of PcD and PcA, respectively. These results indicated that PcDA was an effective ROS generator with the potential to enhance PDT relative to PcD and PcA. PcDA also exhibited a stronger capability to generate ROS than the commercial PS methylene blue (MB) under 655 nm light irradiation. However, the ROS generation capacity of PcDA was considerably lower under 690 nm light irradiation (Figure 4C and Figure S8). In order to better understand this mechanism, white light (400–700 nm) was selected as an irradiation source. As expected, PcDA produced more ROS than pure PcD and pure PcA did under white light irradiation, which was similar to the results observed under 655 nm light irradiation (Figure 4D and Figure S9). These results demonstrated

26924560, 2024, 3, Downloaded from https://onlinelibrary.wiley.com/doi/10.1002/agt2.514 by Ewha Womans University Library, Wiley Online Library on [17/11/2024]. See the Terms and Conditions (https://onlinelibrary.wiley.com/terms-and-conditions) on Wiley Online Library for rules of use; OA articles are governed by the applicable Creative Commons License

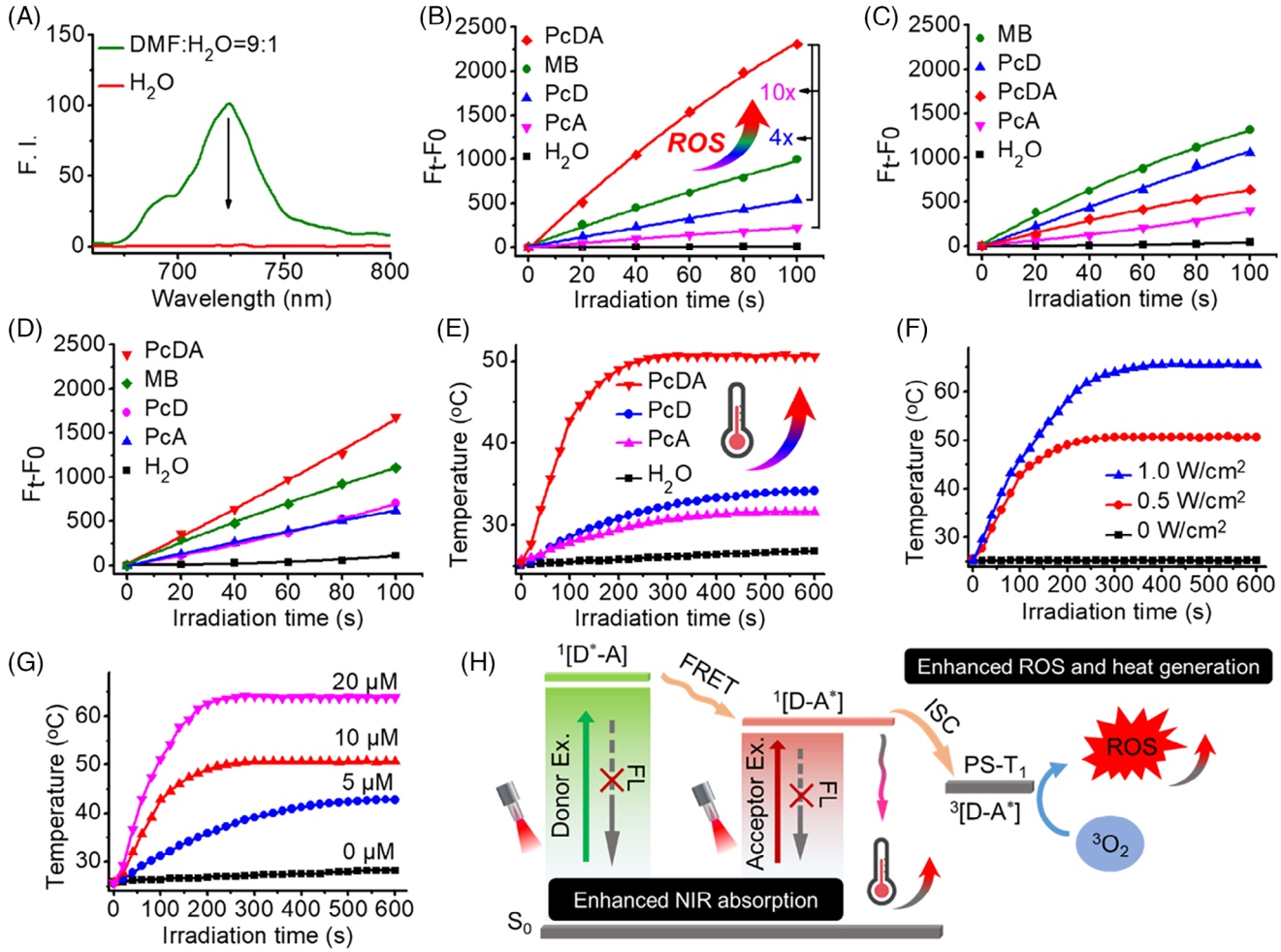


FIGURE 4 Photodynamic and photothermal properties of the nanostructured supramolecular assemblies. (A) Fluorescence (excited at 655 nm) spectra of PcDA (3 μM) in water and in DMF with 10% water. ROS generation of PcA, PcD, PcDA, and MB (all at 4 μM) in water under (B) 655 nm, (C) 690 nm, and (D) white light irradiation (all at 15 mW/cm^2), detected using DCFH-DA as the fluorescent probe. A mixture containing only DCFH-DA was employed as the control. (E) Time-dependent temperatures of PcA, PcD, and PcDA (all at 10 μM) in water upon 655 nm light irradiation for 10 min (0.5 W/cm^2). (F) Temperature elevation of PcDA solutions (10 μM) irradiated with 655 nm light at different power densities (0, 0.5, and 1.0 W/cm^2) for 10 min. (G) Temperature elevation of PcDA solutions at different concentrations (0, 5, 10, and 20 μM) irradiated with 655 nm light at a fixed power density of 0.5 W/cm^2 for 10 min. (H) Illustration of the mechanisms involved in ROS and heat generation due to the FRET effect for PcDA.

that the ROS generation capacity of PcDA was dramatically higher than that of pure PcD and pure PcA after exposure to 655 nm light. We speculated that this was mainly because the FRET effect between PcD and PcA facilitated the utilization of NIR photons, thus enhancing the ROS generation of PcDA, which is crucial to improving its photodynamic effect.

The photothermal performance of PcDA was subsequently evaluated. Pure water was employed as the control. Light at 655 nm was used as the irradiation source because the FRET process in PcDA can be induced at this wavelength. As exhibited in Figure 4E, the temperature of PcDA in water vigorously elevated from 25.5 to 50.6°C ($\Delta T = 25.1$°C) after exposure to 655 nm light (0.5 W/cm^2) for 10 min. By comparison, the temperature of PcD and PcA only increased by only 9 and 6°C under identical environments, respectively. This significant increase in temperature clearly suggests that energy can be transferred from PcD to PcA to generate heat. In addition, as displayed in Figure 4F,G, further investigation demonstrated that the temperature elevation profile of PcDA had a positive correlation with the power density as well as the concentration of PcDA. For example, the temperature of PcDA in an aqueous solution at 20 μM increased to 63.9°C after exposure to 655 nm light for 10 min at 0.5 W/cm^2, indicating the controllable photothermal behavior of PcDA. To further demonstrate the photothermal performance of PcDA, the photothermal conversion efficiency of PcDA was calculated at 15.7% according to the photothermal performance and time constant described in Figure S10, which is much higher than that of pure PcD (3.7%) and pure PcA (3.1%). Furthermore, almost no degradation of PcDA in water was observed after four irradiation-cooling circles, highlighting the outstanding photostability of PcDA (Figure S11). Taken together, these results confirm that the FRET effect between PcD and PcA enhances the NIR absorbance ability and further facilitates the utilization of NIR photons, thus greatly boosting ROS and heat generation by PcDA, suggesting that PcDA could be employed as an efficient PS for combined PDT and PTT (Figure 4H).

2.4 | In vitro phototherapeutic efficacy of PcDA

The synergistic treatment efficacy of PcDA was estimated in vitro. DCFH-DA was used to evaluate the intracellular ROS

26924560, 2024, 3, Downloaded from https://onlinelibrary.wiley.com/doi/10.1002/agt2.514 by Ewha Womans University Library, Wiley Online Library on [17/11/2024]. See the Terms and Conditions (https://onlinelibrary.wiley.com/terms-and-conditions) on Wiley Online Library for rules of use; OA articles are governed by the applicable Creative Commons License

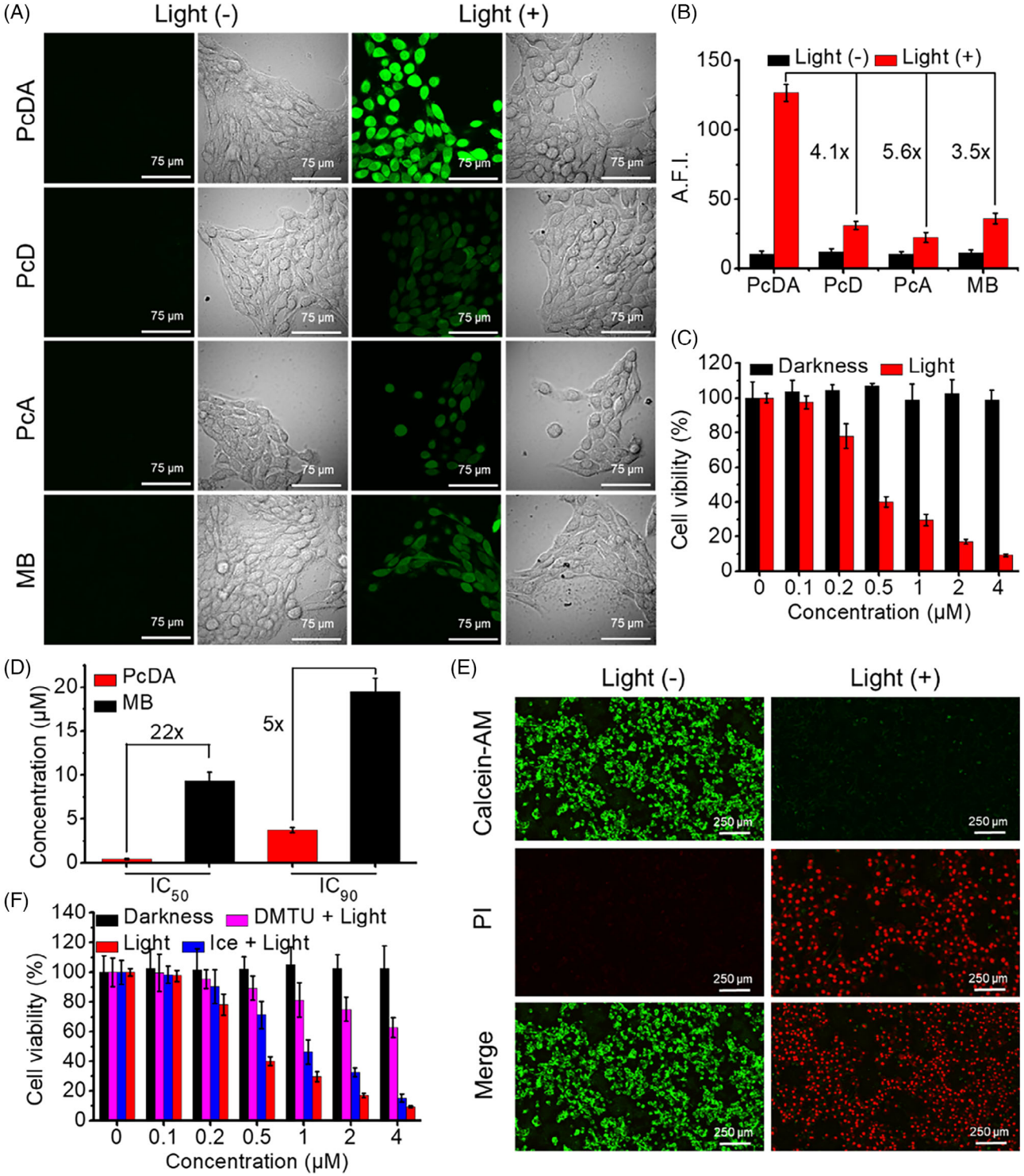


FIGURE 5 In vitro phototherapeutic efficacy of PcDA. (A) Confocal laser scanning microscope (CLSM) images of intracellular ROS generation and (B) quantification of corresponding intracellular ROS generation induced by PcD, PcA, PcDA, and MB (all at 1 μM) in 4T1 cells with or without light irradiation (0.1 W/cm^2, 30 s). DCFH-DA: λ_{ex} = 488 nm, λ_{em} = 510–550 nm. A.F.I., average fluorescence intensity. (C) Cytotoxic effect of PcDA on 4T1 cells in the absence and presence of light irradiation. (D) IC_{50} and IC_{90} values of PcDA and MB. (E) Calcein-AM/PI costaining detected using fluorescence microscopy (scale bar = 250 μm). The cells were divided into two groups: (i) control (PcDA, no light), (ii) PcDA + 655 nm light (0.5 W/cm^2, 10 min). Calcein-AM staining is shown in the green channel, while PI staining is shown in the red channel. (F) Effect of PDT (ice + light) and PTT (DMTU + light) when using PcDA on 4T1 cells. Data were expressed as mean ± SD.

generation of PcDA in mouse breast cancer (4T1) cells. PcD, PcA, and the commercial PS MB were employed as controls. As exhibited in Figure 5A, bright green fluorescence was observed in the PcDA-treated cells under light irradiation, indicating efficient ROS generation. In contrast, PcD, PcA, and MB demonstrated poor intracellular ROS generation, with the intracellular ROS generation of PcDA found to be 4.1-, 5.6-, and 3.5-fold higher than that of PcD, PcA, and MB, respectively (Figure 5B). Furthermore, as shown in Figure S12, the temperature of the PcDA-treated cells reached 52.6°C with light irradiation, much higher than PcD (35.8°C) and PcA (34.6°C).

Motivated by the efficient intracellular ROS and heat generation of PcDA, we assessed its in vitro phototherapeutic

26924560, 2024, 3, Downloaded from https://onlinelibrary.wiley.com/doi/10.1002/agt2.514 by Ewha Womans University Library, Wiley Online Library on [17/11/2024]. See the Terms and Conditions (https://onlinelibrary.wiley.com/terms-and-conditions) on Wiley Online Library for rules of use; OA articles are governed by the applicable Creative Commons License

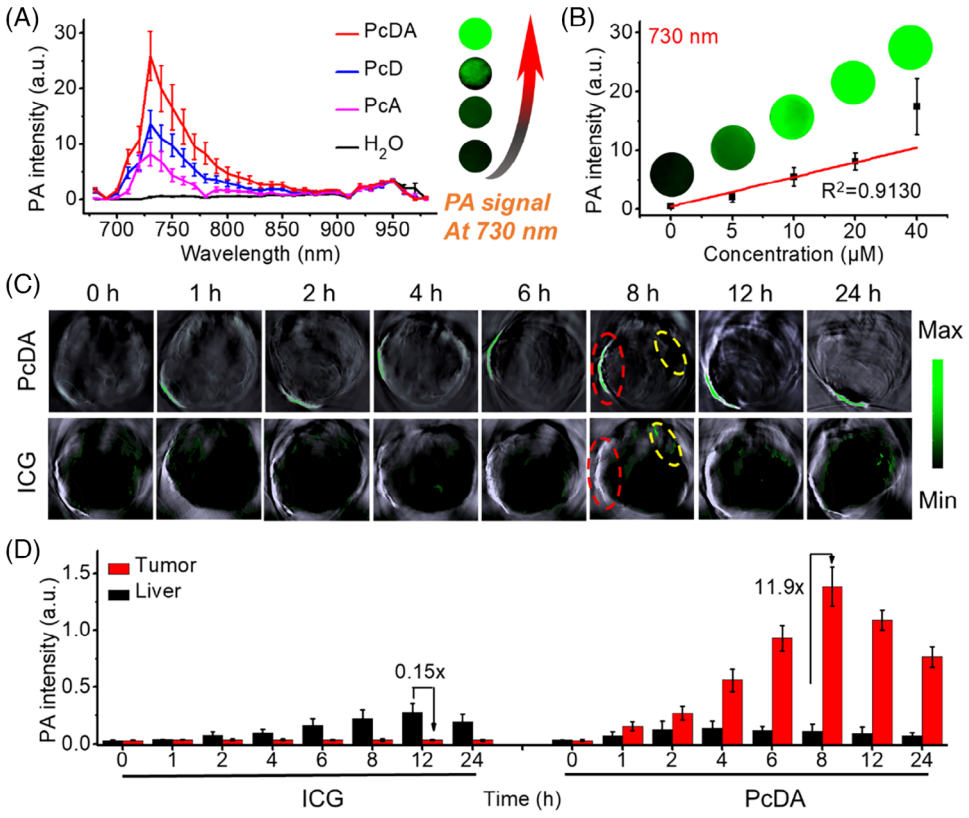


FIGURE 6 In vivo biodistribution of PcDA. (A) In vitro PA amplitude of PcDA at a concentration of 40 μM at various wavelengths. (B) Relationship between the PA signal intensity at 730 nm and the PcDA concentration. The inset shows PA images at different concentrations of PcDA. (C) Representative PA images of H22 tumor-bearing mice before and after the intravenous injection of PcDA (excited at 690 nm) or ICG (excited at 800 nm) at different time points. The red and yellow ellipses denote tumor and liver regions, respectively. (D) Corresponding quantitative analysis of the PA signal intensity at the mice tumor site and in the liver after intravenous injection with PcDA or ICG (dose: 200 μM, 100 μL) at different time points. PA intensity, photoacoustic intensity.

effect via colorimetric 3-(4,5-dimethyl-2-thiazolyl)−2,5-diphenyl-2H-tetrazolium bromide (MTT) assays. As expected, the viability of PcDA-treated cells demonstrated no obvious variation within the measured concentration range without irradiation, indicating that PcDA has good biocompatibility. However, after exposure to light irradiation for 10 min, a dramatic reduction in cell viability was evaluated with a half maximal inhibitory concentration (IC_{50}) of 0.42 ± 0.10 μM, which was 22-fold lower than that of MB (9.31 ± 1.00 μM) (Figure 5D and Figure S13). In addition, the 90% inhibitory concentration (IC_{90}) of MB (19.52 ± 1.80 μM) was 5-fold higher than that of PcDA (3.75 ± 0.50 μM) under identical conditions. The live/dead staining experiment was also conducted to further evaluate the therapeutic efficacy of PcDA. As shown in Figure 5E, almost no green fluorescence was observed in PcDA-treated cells after illumination, providing more evidence that PcDA can effectively kill cells. To further explore the in vitro phototherapeutic mechanisms of PcDA, the cells were treated with the ROS scavenger *N,N′*-dimethylthiourea (DMTU). As exhibited in Figure 5F, compared to the PcDA + light group, the therapeutic efficiency of the PcDA + light + DMTU group was markedly lower, presumably due to the inhibition of PDT. In addition, an ice pack was applied to adjust the temperature of the cells. As expected, the cell suppression efficacy of the PcDA + light + ice group was also lower than the PcDA + light group. These results indicated that PDT and PTT both play a crucial role in the photocytotoxicity of PcDA against cancer cells.

2.5 | In vivo photoacoustic imaging of PcDA

PA imaging and PTT are commonly applied in association for coinstantaneous imaging and treatment applications due to the homology between PA imaging and PTT. Thus, the PA performance of PcDA was investigated. PcD, PcA, and water were used as controls. As exhibited in Figure 6A, consistent with its excellent photothermal effect, PcDA triggered a much stronger PA amplitude than either PcD or PcA. In particular, PcD induced only approximately half the PA amplitude of PcDA, whereas PcA can only produce a weaker PA amplitude than PcD. PA images of PcDA at different concentrations (0–40 μM) become increasingly brighter as the concentration increases, with the PA intensity exhibiting a liner positive correlation with the PcDA concentration (Figure 6B). These results illustrate the feasibility of conducting quantitative analysis based on the PA signal intensity. Then we conducted in vivo PA imaging assays of PcDA (200 μM, 100 μL) in hepatocarcinoma (H22) tumor-bearing mice using intravenous injection. Indocyanine green (ICG) was employed as the control. H22 tumor was selected because the preclinical model is relatively straightforward to construct. Encouragingly, the PA brightness of the tumor region increased progressively after the intravenous injection of PcDA, implying that PcDA can selectively enrich at the tumor site due to the enhanced permeability and retention (EPR) effect (Figure 6C). The PA brightness of the tumor site reached its maximum levels after 8 h of injection, which was approximately 11.9-fold higher than that in the liver (Figure 6D), suggesting that 8 h post-injection was the optimal time for tumor treatment. After this

26924560, 2024, 3, Downloaded from https://onlinelibrary.wiley.com/doi/10.1002/agt2.514 by Ewha Womans University Library, Wiley Online Library on [17/11/2024]. See the Terms and Conditions (https://onlinelibrary.wiley.com/terms-and-conditions) on Wiley Online Library for rules of use; OA articles are governed by the applicable Creative Commons License

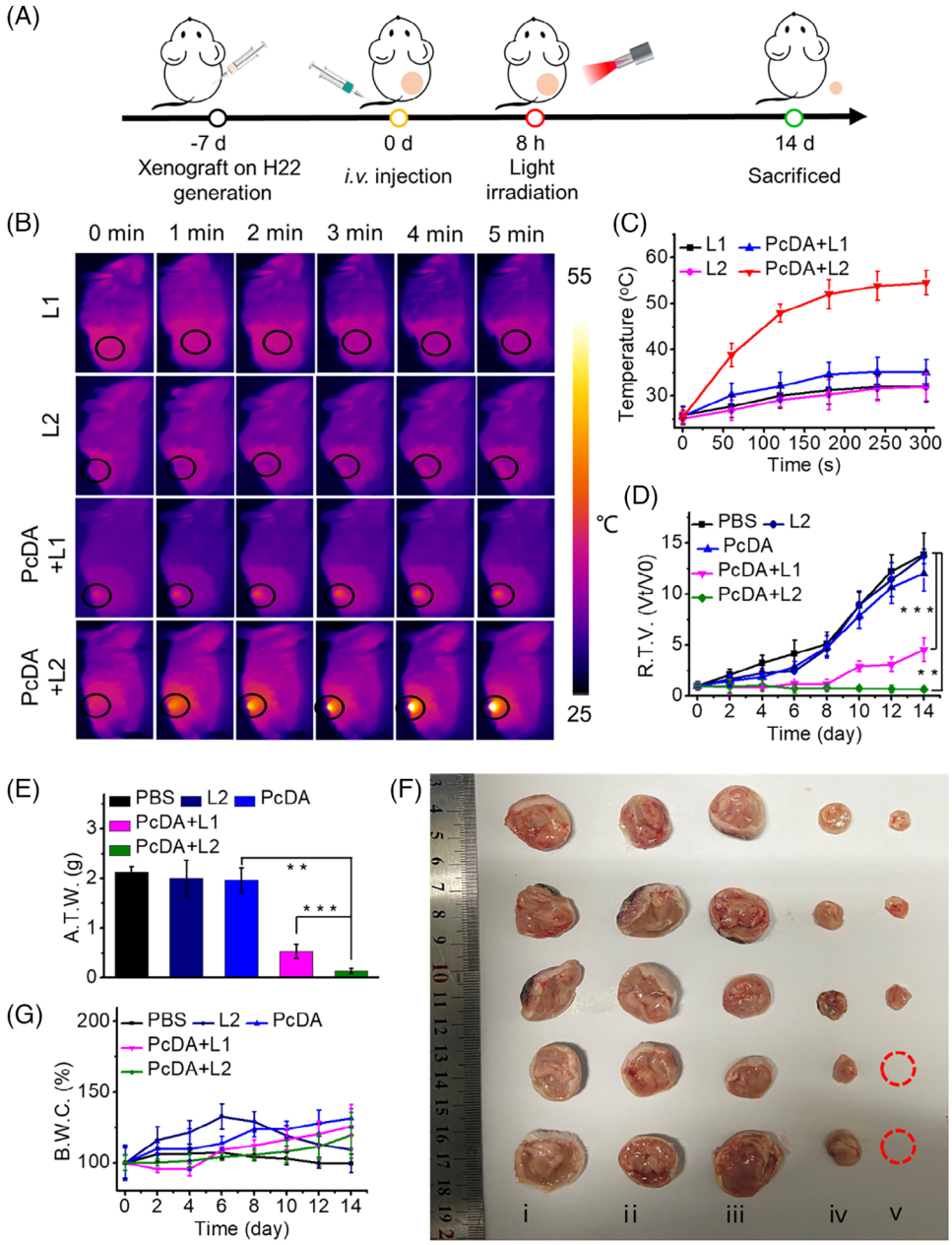


FIGURE 7 In vivo phototherapeutic efficacy of PcDA (200 μM, 100 μL) on H22-bearing mice after intravenous injection. (A) Schematic chart demonstrating the treatment of PcDA on H22 tumor-bearing mice. The orange dot represents the tumor. (B) Infrared thermal imaging of H22 tumor-bearing mice with the indicated treatment. (C) Temperature change curves of H22 tumors in mice with the indicated treatment. (D) Tumor growth curve of H22 tumor-bearing mice after various treatments. R.T.V., relative tumor volume. (E) Average tumor weight and (F) representative tumor images after 14 days of the indicated treatment. (i) PBS, (ii) L2, (iii) PcDA, (iv) PcDA + L1, and (v) PcDA + L2. A.T.W., average tumor weights. (G) Average body weight changes of mice with the indicated treatment. B.W.C., body weight change. Data were expressed as the mean ± SD, $n = 5$. $^{**}p < 0.01$, $^{***}p < 0.001$ determined using the Student's t test.

peak, the PA signal in the tumor region gradually decreased. In contrast, the PA signal intensity of ICG exhibited a negligible increase in the tumor region during the experimental period. As a result, the PA intensity ratio of ICG in the tumor and liver was 0.12 after 8 h following injection, which was 99-fold lower than that of PcDA. These results demonstrated that PcDA had considerable tumor enrichment ability.

2.6 | In vivo phototherapeutic efficacy of PcDA

In vivo phototherapeutic efficacy of PcDA was then assessed in H22 tumor-bearing mice as well (Figure 7A). Tumor-bearing mice were randomly classified into five groups (five mice per group): (1) treated with PBS only (as the control; denoted as PBS); (2) treated with light 2 only (655 nm, 0.5 W/cm^2; denoted as L2); (3) treated with PcDA (200 μM, 100 μL; denoted as PcDA); (4) treated with PcDA (200 μM, 100 μL) followed by light 1 (655 nm, 0.1 W/cm^2) irradiation (denoted as PcDA + L1); (5) treated with PcDA (200 μM, 100 μL) followed by light 2 (655 nm, 0.5 W/cm^2) irradiation (denoted as PcDA + L2). In the L2, PcDA + L1, and PcDA + L2 groups, after corresponding injections for 8 h, each mouse was exposed to light for 5 min. During the irradiation process, infrared images of the living mice were collected at particular time intervals. As exhibited in Figure 7B,C, the rapid elevation in the tumor temperature was clearly observed in the PcDA + L2 group after light irradiation for 5 min, and the eventual tumor temperature of PcDA-injected mice reached

26924560, 2024, 3, Downloaded from https://onlinelibrary.wiley.com/doi/10.1002/agt2.514 by Ewha Womans University Library, Wiley Online Library on [17/11/2024]. See the Terms and Conditions (https://onlinelibrary.wiley.com/terms-and-conditions) on Wiley Online Library for rules of use; OA articles are governed by the applicable Creative Commons License

55°C (ΔT = 30°C). In comparison, the mice treated with L1 and L2, and the mice treated with PcDA + L1, exhibited little change in temperature, implying that only the mice treated with PcDA followed by light 2 irradiation can induce heat generation at the tumor site. Subsequently, the body weight and the tumor volume of the mice in each group were continuously collected for 14 days after the prescribed treatments. As depicted in Figure 7D, the tumor volumes for the mice treated with L2 or PcDA alone were similar to those of the PBS group, confirming that light and PcDA by themselves had a negligible therapeutic effect. On the other hand, the mice treated with PcDA followed by either light 1 or light 2 irradiation demonstrated an obvious antitumor effect for the first 8 days because the tumor growth was significantly suppressed. However, only the mice treated with PcDA followed by light 2 irradiation exhibited consistently inhibited tumor growth all the time, which should benefit from the combined effect of PDT and PTT. Meanwhile, the PcDA + L1 group failed to inhibit tumor growth in the last stages, which should be derived from the effect of PDT alone. The average tumor weights (Figure 7E) and images of tumors (Figure 7F) also confirmed the significant antitumor efficacy of the combination of PDT and PTT.

Body weight is one of the crucial elements for evaluating the side effects of medical treatments because side effects in the post-treatment period may induce a decrease in appetite and discomfort in mice and impact their body weight. As depicted in Figure 7G, the mice treated with PBS and L2 lost some body weight during the course of treatment. However, the mice treated with PcDA did not experience this loss of weight; specifically, the body weight of mice treated with PcDA followed by either light 1 or light 2 irradiation experienced a constant increase during the course of treatments, implying the biocompatibility and applicability of PcDA during the period of therapeutics.

3 | CONCLUSION

In summary, we developed a general strategy for the use of the FRET mechanism in the development of a nanostructured supramolecular phototherapeutic agent for tumor photodynamic and photothermal synergistic therapy. The nanostructured supramolecular phototherapeutic agent (PcDA) was assembled from the quaternary ammonium salt group-tetra-substituted zinc(II) phthalocyanine (PcD) and the sulphonate group-tetra-substituted zinc(II) phthalocyanine (PcA) via anion and cation supramolecular interaction. This approach facilitates more absorbed energy to be employed for amplifying the ROS and heat generation of PcDA, which greatly enhanced the therapeutic efficacy of the treatment and resolved the low photon utilization efficiency of conventional PSs. Furthermore, the nanoassembled PcDA demonstrated an enhanced PA signal compared with pure PcD and pure PcA. Notably, the use of PcDA allowed the tumor to be visualized, with a PA signal-to-liver ratio as high as 11.9, and exhibited remarkable antitumor efficacy through the combined effect of PDT and PTT.

ACKNOWLEDGEMENTS

Xingshu Li would like to thank the National Natural Science Foundation of China (Grant Nos. 22078066 and T2322004). Juyoung Yoon would like to thank the National Research Foundation of Korea (NRF) grant funded by the Korea government (MSIT) (Grant No. 2022R1A2C3005420). DLS was measured using a Nano-ZS (Malvern). The measurement of TEM was performed using a JEM-2100F (JEOL) at the National Research Facilities and Equipment Center (NanoBioEnergy Materials Center) at Ewha Womans University.

CONFLICT OF INTEREST STATEMENT

The authors declare no conflicts of interest.

ETHICS STATEMENT

All animal studies were carried out in compliance with the guidelines of the Animal Ethics Committee of Fuzhou University (2023-SG-001), and also approved by the committee.

ORCID

Juyoung Yoon https://orcid.org/0000-0002-1728-3970

REFERENCES

1. G. Helmlinger, F. Yuan, M. Dellian, R. K. Jain, *Nat. Med.* **1997**, *3*, 177.
2. A. A. Alizadeh, V. Aranda, A. Bardelli, C. Blanpain, C. Bock, C. Borowski, C. Caldas, A. Califano, M. Doherty, M. Elsner, M. Esteller, R. Fitzgerald, J. O. Korbel, P. Lichter, C. E. Mason, N. Navin, D. Pe'er, K. Polyak, C. W. M. Roberts, L. Siu, A. Snyder, H. Stower, C. Swanton, R. G. W. Verhaak, J. C. Zenklusen, J. Zuber, J. Zucman-Rossi, *Nat. Med.* **2015**, *21*, 846.
3. H. J. Knox, J. Hedhli, T. W. Kim, K. Khalili, L. W. Dobrucki, J. Chan, *Nat. Commun.* **2017**, *8*, 1794.
4. M. Zhao, Q. Zeng, X. Li, D. Xing, T. Zhang, *Nano Res*. **2021**, *15*, 716.
5. X. Cao, S. Rao Allu, S. Jiang, M. Jia, J. R. Gunn, C. Yao, E. P. LaRochelle, J. R. Shell, P. Bruza, D. J. Gladstone, L. A. Jarvis, J. Tian, S. A. Vinogradov, B. W. Pogue, *Nat. Commun.* **2020**, *11*, 573.
6. A. Sharma, J. F. Arambula, S. Koo, R. Kumar, H. Singh, J. L. Sessler, J. S. Kim, *Chem. Soc. Rev.* **2019**, *48*, 771.
7. A. P. Castano, P. Mroz, M. R. Hamblin, *Nat. Rev. Cancer* **2006**, *6*, 535.
8. J. P. Celli, B. Q. Spring, I. Rizvi, C. L. Evans, K. S. Samkoe, S. Verma, B. W. Pogue, T. Hasan., *Chem. Rev.* **2010**, *110*, 2795.
9. X. Li, J. F. Lovell, J. Yoon, X. Chen, *Nat. Rev. Clin. Oncol.* **2020**, *17*, 657.
10. X. He, Y. Luo, Y. Li, Y. Pan, R. T. K. Kwok, L. He, X. Duan, P. Zhang, A. Wu, B. Z. Tang, J. Li, *Aggregate* **2023**, *4*, e396.
11. Z. Zhou, J. Song, L. Nie, X. Chen, *Chem. Soc. Rev.* **2016**, *45*, 6597.
12. Y. Y. Zhao, L. Zhang, Z. Chen, B. Y. Zheng, M. Ke, X. Li, J. D. Huang, *J. Am. Chem. Soc.* **2021**, *143*, 13980.
13. Y. Wan, L. H. Fu, C. Li, J. Lin, P. Huang, *Adv. Mater.* **2021**, *33*, 2103978.
14. K. X. Teng, L. Y. Niu, Q. Z. Yang, *J. Am. Chem. Soc.* **2023**, *145*, 4081.
15. Y.-Y. Zhao, Z. Chen, L. Zhang, X.-W. Qin, H. Liu, B.-Y. Zheng, M. Ke, J.-D. Huang, X. Li, *Chem. Eng. J.* **2023**, *474*, 145921.
16. T. Sun, J. Guo, H. Wen, Q. Pei, Q. Wu, D. Hao, C. Dou, Z. Xie, *Aggregate* **2023**, *4*, e362.
17. Y. Liu, P. Bhattarai, Z. Dai, X. Chen, *Chem. Soc. Rev.* **2019**, *48*, 2053.
18. J. F. Lovell, C. S. Jin, E. Huynh, H. Jin, C. Kim, J. L. Rubinstein, W. C. Chan, W. Cao, L. V. Wang, G. Zheng, *Nat. Mater.* **2011**, *10*, 324.
19. Y.-Y. Zhao, H. Kim, V.-N. Nguyen, S. Jang, W. Jun Jang, J. Yoon, *Coord. Chem. Rev.* **2024**, *501*, 215560.
20. X. Zhao, S. Long, M. Li, J. Cao, Y. Li, L. Guo, W. Sun, J. Du, J. Fan, X. Peng, *J. Am. Chem. Soc.* **2020**, *142*, 1510.
21. X. Liu, Y. Duan, B. Liu, *Aggregate* **2021**, *2*, 4.
22. R. Weissleder, M. J. Pittet, *Nature* **2008**, *452*, 580.
23. Lihong V. Wang, S. Hu, *Science* **2012**, *335*, 1458.
24. T. Liu, Y. Chen, H. Wang, M. Cui, J. Zhang, W. Zhang, P. Wang, *Adv. Healthc. Mater.* **2023**, *12*, 2202817.
25. H. Hu, H. Wang, Y. Yang, J. F. Xu, X. Zhang, *Angew. Chem. Int. Ed.* **2022**, *61*, 202200799.
26. J. Zou, P. Wang, Y. Wang, G. Liu, Y. Zhang, Q. Zhang, J. Shao, W. Si, W. Huang, X. Dong, *Chem. Sci.* **2019**, *10*, 268.

26924560, 2024, 3, Downloaded from https://onlinelibrary.wiley.com/doi/10.1002/agt2.514 by Ewha Womans University Library, Wiley Online Library on [17/11/2024]. See the Terms and Conditions (https://onlinelibrary.wiley.com/terms-and-conditions) on Wiley Online Library for rules of use; OA articles are governed by the applicable Creative Commons License

27. H. B. Cheng, X. Cao, S. Zhang, K. Zhang, Y. Cheng, J. Wang, J. Zhao, L. Zhou, X. J. Liang, J. Yoon, *Adv. Mater.* **2023**, *35*, 2207546.
28. J. Hu, H. Luo, Q. Qu, X. Liao, C. Huang, J. Chen, Z. Cai, Y. Bao, G. Chen, B. Li, W. Cui, *ACS Appl. Mater. Interfaces* **2020**, *12*, 42511.
29. Z. Shi, X. Han, W. Hu, H. Bai, B. Peng, L. Ji, Q. Fan, L. Li, W. Huang, *Chem. Soc. Rev.* **2020**, *49*, 7533.
30. J. Wang, G. Zhu, M. You, E. Song, M. I. Shukoor, K. Zhang, M. B. Altman, Y. Chen, Z. Zhu, C. Z. Huang, W. Tan, *ACS Nano* **2012**, *6*, 5070.
31. H. Li, H. Kim, J. Han, V. N. Nguyen, X. Peng, J. Yoon, *Aggregate* **2021**, *2*, e51.
32. Q. Wan, R. Zhang, Z. Zhuang, Y. Li, Y. Huang, Z. Wang, W. Zhang, J. Hou, B. Z. Tang, *Adv. Funct. Mater.* **2020**, *30*, 2002057.
33. L. Zhang, Y. Geng, L. Li, X. Tong, S. Liu, X. Liu, Z. Su, Z. Xie, D. Zhu, M. R. Bryce, *Chem. Sci.* **2021**, *12*, 5918.
34. J. Shao, H. Xie, H. Huang, Z. Li, Z. Sun, Y. Xu, Q. Xiao, X. F. Yu, Y. Zhao, H. Zhang, H. Wang, P. K. Chu, *Nat. Commun.* **2016**, *7*, 12967.
35. X. Yang, D. Wang, J. Zhu, L. Xue, C. Ou, W. Wang, M. Lu, X. Song, X. Dong, *Chem. Sci.* **2019**, *10*, 3779.
36. C. Ji, L. Lai, P. Li, Z. Wu, W. Cheng, M. Yin, *Aggregate* **2021**, *2*, e39.
37. S. Shao, J. Geng, H. Ah Yi, S. Gogia, S. Neelamegham, A. Jacobs, J. F. Lovell, *Nat. Chem.* **2015**, *7*, 438.
38. Q. Zou, M. Abbas, L. Zhao, S. Li, G. Shen, X. Yan, *J. Am. Chem. Soc.* **2017**, *139*, 1921.
39. X. Ma, Y. Zhao, *Chem. Rev.* **2015**, *115*, 7794.
40. W. J. Guo, T. Peng, W. Zhu, S. Ma, G. Wang, Y. Li, B. Liu, H. Q. Peng, *Aggregate* **2022**, *4*, e297.
41. J. Tian, L. Xia, J. Wu, B. Huang, H. Cao, W. Zhang, *ACS Appl. Mater. Interfaces* **2020**, *12*, 32352.
42. K. X. Teng, L. Y. Niu, Q. Z. Yang, *Chem. Sci.* **2022**, *13*, 5951.
43. J. Zhou, G. Yu, F. Huang, *Chem. Soc. Rev.* **2017**, *46*, 7021.
44. H. Yang, B. Yuan, X. Zhang, O. A. Scherman, *Acc. Chem. Res.* **2014**, *47*, 2106.
45. P. C. Lo, M. S. Rodriguez-Morgade, R. K. Pandey, D. K. P. Ng, T. Torres, F. Dumoulin, *Chem. Soc. Rev.* **2020**, *49*, 1041.
46. Y.-Y. Zhao, J.-Y. Chen, J.-Q. Hu, L. Zhang, A.-L. Lin, R. Wang, B.-Y. Zheng, M.-R. Ke, X. Li, J.-D. Huang, *Dyes Pigm.* **2021**, *189*, 109270.
47. X. Li, X. H. Peng, B. D. Zheng, J. Tang, Y. Zhao, B. Y. Zheng, M. R. Ke, J. D. Huang, *Chem. Sci.* **2018**, *9*, 2098.
48. X. Li, C. Y. Kim, S. Lee, D. Lee, H. M. Chung, G. Kim, S. H. Heo, C. Kim, K. S. Hong, J. Yoon, *J. Am. Chem. Soc.* **2017**, *139*, 10880.
49. H. Liu, X.-Y. Li, X. Li, J.-D. Huang, *Green Chem. Eng.* **2022**, *4*, 399.
50. K. Zheng, X. Liu, M. Li, S. Zhou, C. Ding, *Anal. Chem.* **2022**, *94*, 15067.
51. Z. Wang, T. Jia, Q. Sun, Y. Kuang, B. Liu, M. Xu, H. Zhu, F. He, S. Gai, P. Yang, *Biomaterials* **2020**, *228*, 119569.
52. M. Li, S. Long, Y. Kang, L. Guo, J. Wang, J. Fan, J. Du, X. Peng, *J. Am. Chem. Soc.* **2018**, *140*, 15820.
53. L. Huang, Z. Li, Y. Zhao, J. Yang, Y. Yang, A. I. Pendharkar, Y. Zhang, S. Kelmar, L. Chen, W. Wu, J. Zhao, G. Han, *Adv. Mater.* **2017**, *29*, 1604789.
54. Y. Zou, S. Long, T. Xiong, X. Zhao, W. Sun, J. Du, J. Fan, X. Peng, *ACS Cent. Sci.* **2021**, *7*, 327.
55. F. Scholkmann, S. Kleiser, A. J. Metz, R. Zimmermann, J. Mata Pavia, U. Wolf, M. Wolf, *Neuroimage* **2014**, *85*, 6.

SUPPORTING INFORMATION

Additional supporting information can be found online in the Supporting Information section at the end of this article.

How to cite this article: Y.-Y. Zhao, X. Zhang, Z. Chen, Y. Xu, H. Kim, H. Jeong, Y. R. Lee, J. Lee, X. Li, J. Yoon, *Aggregate* **2024**, *5*, e514. https://doi.org/10.1002/agt2.514

26924560, 2024, 3, Downloaded from https://onlinelibrary.wiley.com/doi/10.1002/agt2.514 by Ewha Womans University Library, Wiley Online Library on [17/11/2024]. See the Terms and Conditions (https://onlinelibrary.wiley.com/terms-and-conditions) on Wiley Online Library for rules of use; OA articles are governed by the applicable Creative Commons License